



**HAL**  
open science

# Influence of solidification conditions on chemical heterogeneities and dislocations patterning in additively manufactured 316L stainless steel

Sylvain Dépinoy

► **To cite this version:**

Sylvain Dépinoy. Influence of solidification conditions on chemical heterogeneities and dislocations patterning in additively manufactured 316L stainless steel. *Materialia*, 2022, 24, pp.101472. 10.1016/j.mtla.2022.101472 . hal-03709672

**HAL Id: hal-03709672**

**<https://hal.science/hal-03709672>**

Submitted on 22 Jul 2024

**HAL** is a multi-disciplinary open access archive for the deposit and dissemination of scientific research documents, whether they are published or not. The documents may come from teaching and research institutions in France or abroad, or from public or private research centers.

L'archive ouverte pluridisciplinaire **HAL**, est destinée au dépôt et à la diffusion de documents scientifiques de niveau recherche, publiés ou non, émanant des établissements d'enseignement et de recherche français ou étrangers, des laboratoires publics ou privés.



Distributed under a Creative Commons Attribution - NonCommercial 4.0 International License

# **Influence of solidification conditions on chemical heterogeneities and dislocations patterning in additively manufactured 316L stainless steel**

Sylvain Dépinoy

Mines Paris, PSL University, MAT - Centre des Matériaux, CNRS UMR 7633, BP 87, 91003 Evry, France  
sylvain.depinoy@minesparis.psl.eu

**Keywords:** Solidification, dendrites, dislocations, microsegregations, 316L

## **Abstract**

The dendritic substructure of 316L stainless steel processed by Laser Powder Bed Fusion (L-PBF) is experimentally investigated on three specimens built with significantly different scanning speeds and solidification cooling rates. Microstructural features of interest are misorientations between dendrites, gradients of chemical composition and dislocations structures. Similar amplitudes of chemical heterogeneities are found for all three samples, possibly related to the conjunction of relatively low variations of solidification rates and large partition coefficients for the considered solute elements. No crystalline misorientations between neighboring dendrites are observed, implying that interdendritic dislocations are not geometrically necessary dislocations stemming from solidification but arise from thermomechanical straining during post-solidification cooling. Dislocations patterning appear to be closely correlated to the periodicity of microsegregations, hinting at an effect of the local chemistry. No simple Hall-Petch-like effect of the dendrite size is observed on compression tests, possibly due to different strengthening mechanisms depending on the dislocations patterning.

## **Introduction**

Laser Powder Bed Fusion is known to induce a metastable intragranular substructure in several materials, e.g. austenitic stainless steels [1], aluminum alloys [2], nickel-based superalloys [3] and high entropy alloys [4]. Past years have seen extensive scientific efforts aiming at understanding and controlling

the formation of this substructure in 316L stainless steels due to its effect on mechanical properties or corrosion resistance [5]. In this framework, additive manufacturing would not only be a mean of producing complex geometrical parts but also a way to enhance final properties by designing otherwise unobtainable microstructures.

The intragranular substructure in 316L stainless steel consists of cylindrical domains of submicrometric diameter separated by chemically enriched boundaries and dense dislocations walls. Subdomains are elongated in a  $\langle 001 \rangle$  direction and as such correspond to solidification dendrites [6]. Chemical heterogeneities therefore stem from solidification, where the first solid germs (the dendrite tip) and the last droplets of liquid to solidify (interdendritic boundaries) exhibit different chemical compositions due to differences in solute solubility in liquid and solid phases. Spatial periodicity of microsegregations is thus given by the interdendritic spacing, itself related to the solidification cooling rate [7,8]. Interdendritic boundaries in 316L processed by L-PBF are enriched in chromium, nickel and molybdenum [9], consistently with a metastable austenitic solidification arising from the phase selection mechanism associated with rapid solidification [10–12]. The lack of secondary dendrite arms, resulting in “cell-like dendrites”, can be explained by the relatively narrow solidification interval [13]. It is known from classical solidification theory that the magnitude of solute redistribution during solidification mainly depends on the solidification rate  $V$  through two mechanisms [14]: constitutional undercooling, which sets the composition of the dendrite tip [15], and solute trapping, upon which solute partition coefficients tend towards unity with increasing  $V$  [16,17]. Other factors such as temperature gradients or convection flows can also be of importance [18,19]. On the other hand, the origin of dislocations in additively manufactured materials has been the subject of several theories over the years. Earliest studies attributed the existence of interdendritic dislocations in 316L to lattice distortion resulting from local enrichment in molybdenum [1], although this is contradicted by observations of dislocations structures in molybdenum-free 304L [20] or high-purity copper [21]. A second theory postulates that interdendritic dislocations are geometrically necessary dislocations (GNDs) accommodating crystalline misorientations between neighboring dendrites [22]. While such dendritic subgrains have been reported in welding [23], the very small misorientations between dendrites [24–26] and observations of intradendritic dislocations cells [9,25] in 316L processed by L-PBF would tend to disprove this theory. A third theory, originally put forth by Vilaro et al. [27], is that

dislocations are generated through the thermomechanical cycles experienced by the part during its construction. Bertsch et al [25] confirmed this theory through a well-designed set of experiments resulting in different dislocation patterns as a function of the process parameters. Observations of dislocations substructures on single tracks [28,29] further show that most of these thermomechanical stresses arises during the first cooling step after solidification, and that subsequent heating-cooling cycles are of less importance.

There are, however, few thorough investigations on the dependency of the final substructure on L-PBF process conditions. Despite arising from well-known phenomena, precise quantification of L-PBF-induced microsegregations are indeed lacking in the literature, where most studies only report qualitative or semi-quantitative chemical characterizations, i.e. element mappings or line-scans using energy dispersive X-ray spectroscopy (EDS) in scanning transmission electron microscopy (STEM) [24,30–34]. Consequently, there is little data on the effect of L-PBF process parameters on the final chemical heterogeneities. Similarly, there are very few studies dedicated to the effect of L-PBF process parameters on the organization of dislocations structures in as-built materials, and interrogations remain about the origin of the preferential localization of dislocations at interdendritic boundaries. Finally, while there is a general agreement that the high yield strength of additively manufactured 316L is caused by the intragranular substructure, the strengthening mechanisms at play remain unclear. Two theories are usually put forth: an Hall-Petch-like effect of dendrites [35,36] or a hardening related to the high dislocations density [37].

The present study aims at systematically investigating the effect of solidification conditions on the chemical heterogeneities and dislocations structures in 316L processed by L-PBF. To this end, three specimens built with different sets of processing parameters are characterized. The dendritic substructure, dislocations patterning and chemical heterogeneities are experimentally investigated by means of Transmission Electron Microscopy (TEM), EDS quantifications, Backscattered Electrons (BSE) Scanning Electron Microscopy (SEM) and Electron Backscattered Diffraction (EBSD). The relationship between the solidification conditions and the final substructure is subsequently discussed, and the resulting mechanical properties are briefly assessed.

## 1. Experimental procedure

### 1.1 Materials of study

Three 30×20×13 mm<sup>3</sup> specimens, hereafter referred to specimens 1 to 3, were built on a Concept Laser M2 machine using a commercial 316L stainless steel powder supplied by Concept Laser. Different sets of process parameters corresponding to different surface energies  $E_s = (4/\pi) \times (P/V_b\varphi)$  were used, where  $P$  is the laser power,  $V_b$  the scan speed, and  $\varphi$  the spot diameter (Table 1). Parameters used for specimens 1 and 2 are not representative of industrial conditions and were selected to probe a wide range of solidification conditions. Hatch spacing was set to 160  $\mu\text{m}$ , 110  $\mu\text{m}$  and 75  $\mu\text{m}$  for samples 1 to 3, respectively, corresponding to a 33% overlap between adjacent tracks for all three conditions. All specimens were built with a slice thickness of 50  $\mu\text{m}$  following a bidirectional scanning strategy with no rotation between layers. An interlayer time of 60 s was applied to minimize the heat accumulation in the consolidated part during construction to ensure the homogeneity of thermal history throughout the built [38,39] and to reduce solid-state diffusion. In the following, the scanning direction and the building direction will be referred to as the  $x$ - and  $z$ -axis, respectively.

Mean chemical compositions of the studied parts were measured by Electron Micro Probe Analysis and were found to be close to the nominal powder composition given by the supplier, as shown in Table 2. Note that slightly higher amounts of nickel and molybdenum and lower amounts of manganese and chromium are observed for specimen 1. This is believed to be related to the vaporization of these last two elements due to the comparatively higher melt pool temperature resulting from the high surface energy [40,41].

*Table 1: Processing parameters for the three studied specimen*

Specimen number	1	2	3
$P$ (W)	133	180	150
$V_b$ (mm/s)	66.5	360	750
$\varphi$ (mm)	0.2	0.2	0.1
$E_s$ (J/mm <sup>2</sup> )	12.7	3.2	2.5

*Table 2: Nominal powder composition supplied by the manufacturer, determined by XRF spectroscopy, combustion analysis and loss on drying, and final specimen composition as measured by an average of 15 EPMA.*

wt%	C	Si	Cr	Mn	Fe	Ni	Mo
Nominal	0.02	0.65	17.9	1.40	bal.	12.8	2.4

Sample 1	-	0.84	17.3	0.64	65.3	13.2	2.7
Sample 2	-	0.76	18.0	0.94	65.1	12.8	2.4
Sample 3	-	0.76	18.2	1.00	65.1	12.7	2.3

## 1.2 Microstructural characterizations

Characterizations of the substructure were performed on thin foils taken on the  $x$ - $y$  plane and prepared as follows. A 200  $\mu\text{m}$  thick disk was cut close to the top surface of a 3 mm diameter cylinder machined following the building direction, grinded down to a thickness of 100  $\mu\text{m}$ , and electrolytically thinned using a 45% butoxyethanol, 45% acetic acid, 10% perchloric acid solution with a 40 V tension at 0 °C. TEM and STEM observations were conducted on a FEI Tecnai F20 FEG-TEM with a 200 kV acceleration voltage. Prior to TEM observations, thin foils underwent a plasma cleaning for 120 s. EDS spectra were acquired using a Bruker XFlash 6T | 60 detector with a counting time of 30 s. 208 data points (i.e. a  $13 \times 16$  square grid) were acquired per specimen on an area of interest of  $3.8 \times 3.8 \mu\text{m}^2$ ,  $2.7 \times 2.7 \mu\text{m}^2$  and  $1.4 \times 1.4 \mu\text{m}^2$  for specimen 1 to 3, respectively, encompassing approximately 10-15 solidification dendrites belonging to a single grain. SEM observations were conducted on a FEI Nova NanoSEM 450 SEM using an acceleration voltage of 5 kV. EBSD analyses were performed with an EDAX OIM Hikari camera, using an acceleration voltage of 20 kV with a step size of 50 nm. Post-processing of EBSD data was performed using the MTEX toolbox [42]. EBSD and SEM observations were performed on the same area located in the immediate vicinity of areas analyzed by TEM and EDS. All observations and analyses were carried on dendrites cross-sectioned close to a  $\langle 001 \rangle$  direction with respect to the incident beam, and the mean dendrite diameter  $\lambda$  was determined by direct measurement of  $\sim 10$  and  $\sim 200$  dendrites from SEM and STEM observations, respectively.

Study of large-scale microstructures was conducted by means of optical microscopy and EBSD. Specimens were first cut by electrical discharge machining along the  $y$ - $z$  plane at the center of the built part before undergoing standard metallographic preparation followed by OPS polishing. Prior to optical microscopy, specimens were etched at 10 V for 1 minute on a 10% solution of oxalic acid in water. EBSD analyses were performed with an acceleration voltage of 20 kV and a step size of 0.5  $\mu\text{m}$ .

### 1.3 Post-processing of STEM-EDS data

STEM-EDS data were post-processed using the Cliff-Lorimer method implanted in the Esprit 2.2 software. A detailed discussion on the reliability of the STEM-EDS data and of the post-processing scheme can be found in the Appendix. It is concluded that large uncertainties associated with the absolute concentration  $C_k^i$  of an element  $i$  at the EDS point location  $k$  are greatly reduced when one considers the nondimensional concentrations  $C_k^i/\bar{C}^i$ , where  $\bar{C}^i$  is the average concentration of  $i$  over the whole dataset. Silicon and manganese concentrations were deemed unreliable, the former due to its high absorptivity and the latter due to its low concentration and pathological overlap with iron and chromium energy rays. As such, they were included in the quantification scheme but excluded from further post-treatment.

Segregation profiles were reconstructed using the rank sort (RS) method [43] using nondimensional concentrations. The RS method is as follows: for each composition site  $k$ , the nondimensional concentration  $C_k^i/\bar{C}^i$  of a given element  $i$  is assigned a rank  $r_k^i$  such that for element that segregate to the liquid the minimum concentration has a rank of 1 and the maximum concentration a rank of  $n$ , where  $n$  is the total number of measurements. The average rank value  $R_k$  of the point location is taken as the average of  $r_k^i$  for all elements  $i$ , and the corresponding solid fraction  $f_s(k)$  is given by  $f_s(k) = (R_k - 0.5)/n$  [43]. In this work, solid fractions are converted to nondimensional lengths  $2x/\lambda$ , where  $\lambda$  is the interdendritic spacing.

### 1.4 Thermokinetic calculations

Thermokinetic calculations were performed with the ThermoCalc software version 2017a using the TCFE9 and MOBFE4 databases. Solid-state diffusion calculations were performed with Dictra over a length corresponding to half the dendrite diameter assuming a closed cylindrical system. The total length of the system was discretized into 500 points, and an automatic time stepping was used. Initial composition profiles were taken as the Scheil-Gulliver profile determined with ThermoCalc for the liquid/austenite system using the nominal powder composition (Table 2).

## 1.5 Compression tests

Uniaxial compression tests were performed with an Instron 5982 on  $\Phi 5 \times 8 \text{ mm}^3$  cylinders machined following the building direction. A traverse speed of 0.5 mm/min was used, corresponding to a strain rate of approximately  $10^{-3} \text{ s}^{-1}$ . No extensometers were used and strain was measured as follows. The traverse displacement during the compression tests was recorded, and a complementary test with no specimen was performed in order to determine the contribution of the machine to the measured displacements. Recorded displacements were then corrected and divided by the height of the specimens. Three tests were performed for specimens 1 and 2, and two tests for specimen 3. Yield strength was determined as the 0.2% deformation offset yield point using the Young modulus as determined from true stress-true strain curves between 230 MPa and 430 MPa.

## 2. Results and discussions

### 2.1 Grain structures

Figure 1 shows optical micrographs, orientation maps and inverse pole figures of the three specimens taken along the  $y$ - $z$  plane. While increasing the surface energy leads to larger molten pools, all three samples exhibit a similar microstructure consisting of an alternation of large and small austenite grains, oriented close to the  $\langle 101 \rangle$  and  $\langle 001 \rangle$  directions with respect to the building direction and  $\langle 001 \rangle$  and  $\langle 111 \rangle$  directions with respect to the scanning direction, respectively. Such microstructures have been well documented for face-centered-cubic materials such as 316L stainless steel [44–47] or Inconel 718 [48] and stem from the growth competition between grains, i.e. the competition between epitaxial growth and the preferential growth direction of dendrites with respect to the thermal gradient [49]. At the center of the melt pool, the thermal gradient is closely aligned with the building direction such that growth is promoted for dendrites oriented close to the  $\langle 001 \rangle$  direction. On the melt pool sides, growth occurs with a  $\pm 45^\circ$  angle with respect to the building direction, resulting in grains oriented in the  $\langle 101 \rangle$  direction due to the cubic symmetry of the austenite lattice.

*Figure 1: (a) Optical micrographs showing the melt pools arrangement, (b) orientation maps with the reference axis set as the building direction, (c) inverse pole figures taken along the building and scanning directions for specimen 1 (left), 2 (middle) and 3 (right).*

## **2.2 Dendritic structures**

Figure 2 shows STEM observations of the dendritic structure for the three specimens. EBSD analyses along with SEM observations are gathered in Figure 3 to 6 for specimens 1 to 3, respectively. Increasing the surface energy leads to larger dendrites: average dendrite diameters measured by STEM are  $0.80 \pm 0.07 \mu\text{m}$ ,  $0.65 \pm 0.02 \mu\text{m}$  and  $0.30 \pm 0.02 \mu\text{m}$  for specimens 1 to 3, respectively. Very similar values are found for specimens 2 and 3 by SEM, respectively  $0.60 \pm 0.16 \mu\text{m}$  and  $0.30 \pm 0.04 \mu\text{m}$ , while a wider range of dendrite diameters were observed for specimen 1, from  $0.80 \mu\text{m}$  to  $1.10 \mu\text{m}$ . These results confirm that the different sets of processing parameters resulted in different solidification conditions with corresponding cooling rates of  $0.5\text{-}1 \times 10^6 \text{ }^\circ\text{C/s}$ ,  $2 \times 10^6 \text{ }^\circ\text{C/s}$  and  $2 \times 10^7 \text{ }^\circ\text{C/s}$  for specimens 1 to 3 according to the empirical equation proposed by [7]. Interdendritic boundaries as measured by SEM were found to represent approximately 10% to 15% of  $\lambda$  regardless of the surface energy. These boundaries correspond to the chemically enriched areas that appear brighter on BSE-SEM images.

STEM observations as well as EBSD orientation and IQ maps show that high- and low-angle grain boundaries follow interdendritic boundaries, such that grains and subgrains consist of packets of cells sharing similar crystalline orientations. Such observations were already reported by [24,50] and show that these subgrains are unlikely to stem from dynamic recovery as proposed e.g. by [51]. Misorientations between neighboring cells belonging to a single packet are found to be within the measurement noise, i.e. less than  $0.5\text{-}1 \text{ }^\circ$  regardless of the dendrite size. Similar interdendritic misorientations are reported by several authors for 316L processed by L-PBF [24–26] and for the more general case of directionally grown face-centered-cubic single crystals [52]. These small misorientations can be explained by the epitaxial growth responsible for the texture development of the specimens. Melt pool boundaries are characterized by large thermal gradients and low solidification rates [53], leading to the growth of a plane front following a symmetrically equivalent crystalline direction with respect to the local orientation of the unmelted metal. Such chemically homogeneous planar fronts at a melt pool boundary were observed in this study (Figure 6), consistently with the literature for stainless steels processed by electron beam welding [10] and L-PBF [54,55]. As solidification progresses, the planar interface quickly decays into an array of dendrites that

inherit its crystalline orientation. Thus, dendrites originating from a plane front of a given orientation are expected to be weakly misoriented with respect to each other.

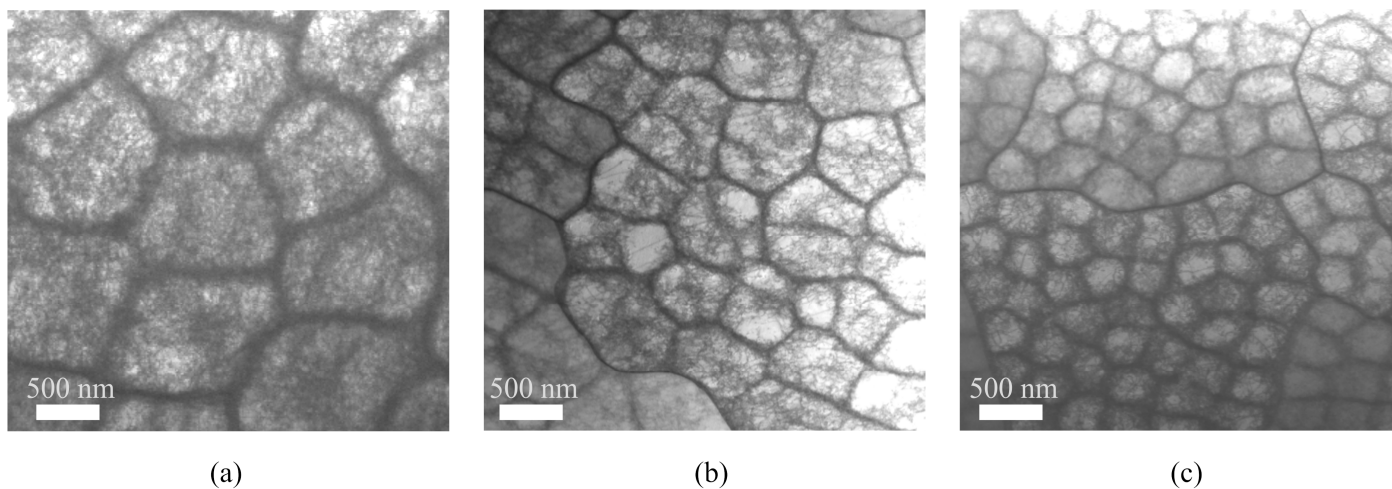


Figure 2: Bright-field STEM observations of dendritic structure for (a) specimen 1, (b) specimen 2 and (c) specimen 3.

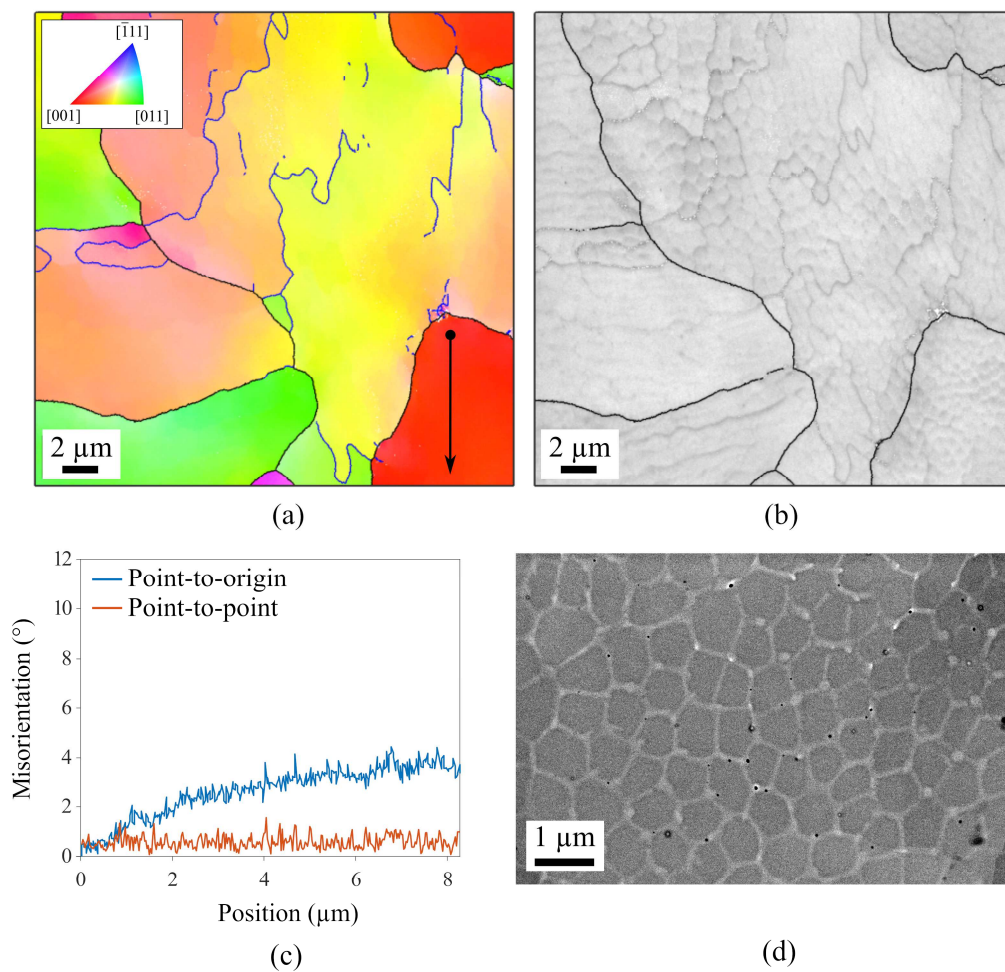


Figure 3: (a) Orientation and (b) Image Quality maps of specimen 1, (c) point-to origin and point-to-point misorientation corresponding to the black arrow in (a), (d) BSE-SEM image of the dendritic structure. Black lines and blues lines symbolize HAGB ( $>15^\circ$ ) and LAGB ( $>2^\circ$ ), respectively.

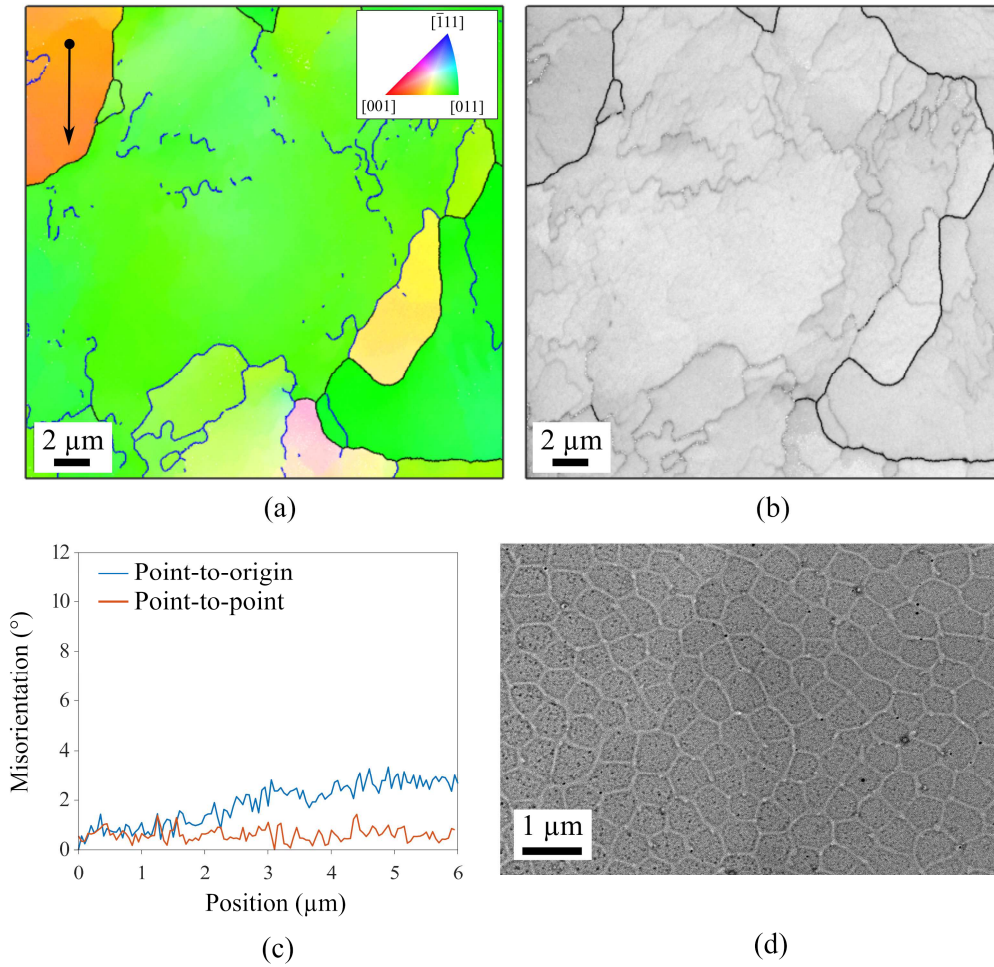


Figure 4: (a) Orientation and (b) Image Quality maps of specimen 2, (c) point-to origin and point-to-point misorientation corresponding to the black arrow in (a), (d) BSE-SEM image of the dendritic structure. Black lines and blues lines symbolize HAGB ( $>15^\circ$ ) and LAGB ( $>2^\circ$ ), respectively.

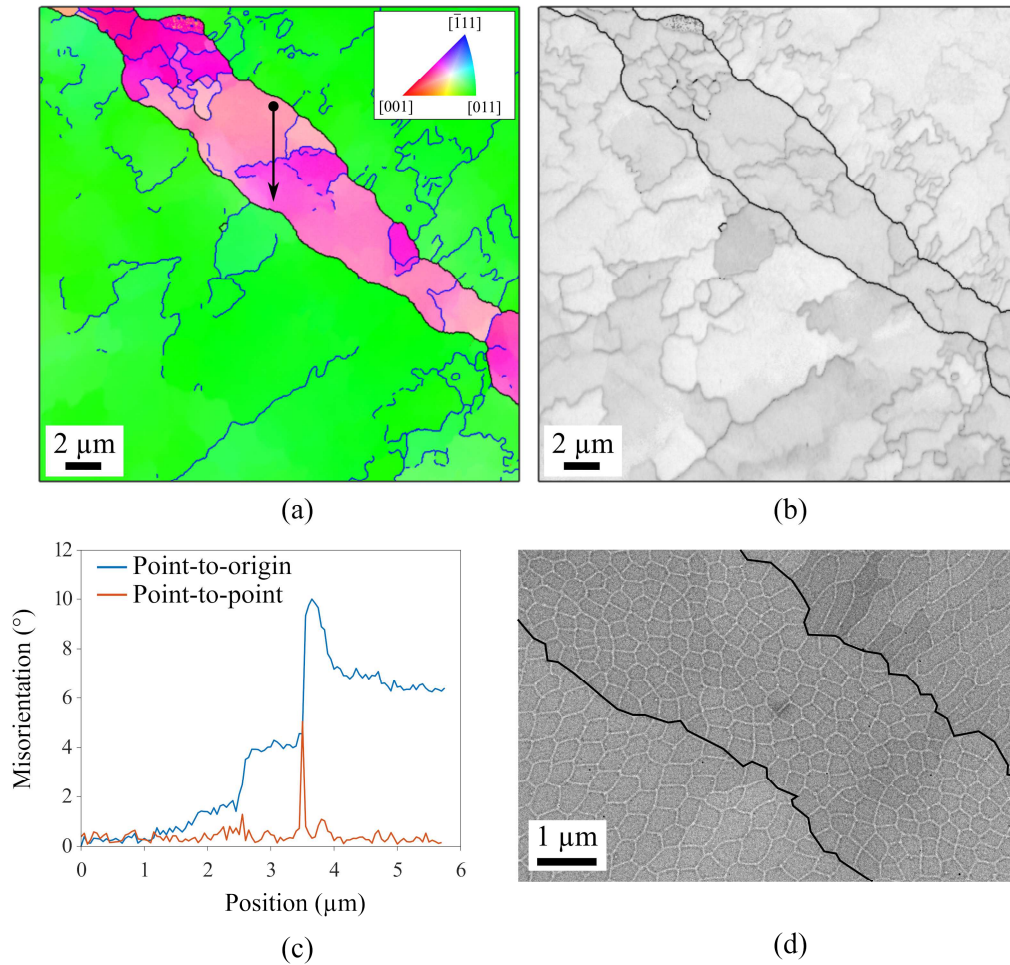


Figure 5 : (a) Orientation and (b) Image Quality maps of specimen 3, (c) point-to origin and point-to-point misorientation corresponding to the black arrow in (a), (d) BSE-SEM image of the dendritic structure. Black lines and blue lines symbolize HAGB ( $>15^\circ$ ) and LAGB ( $>2^\circ$ ), respectively.

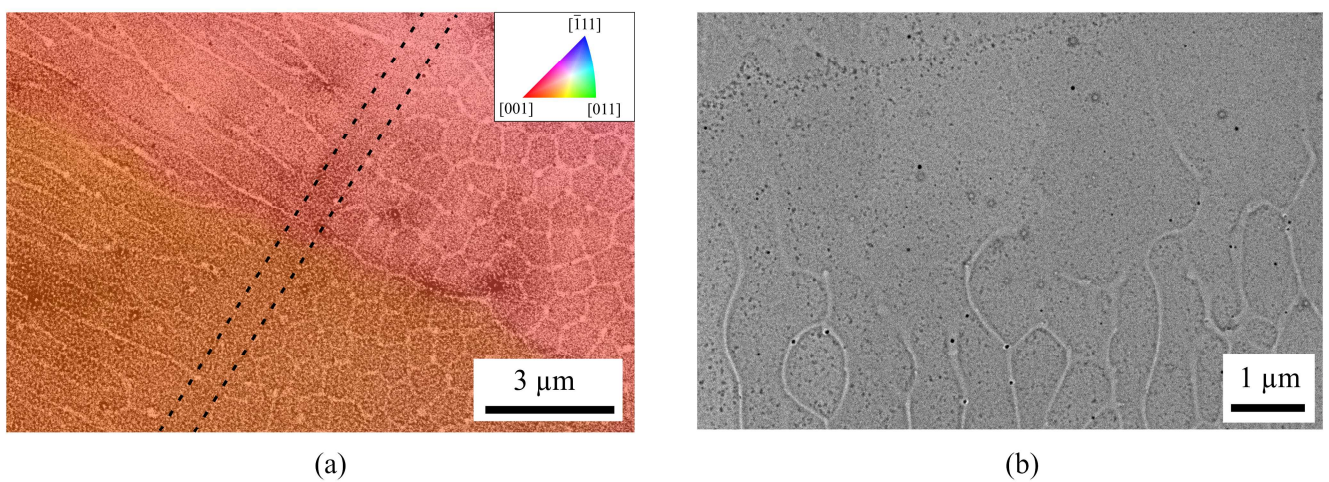


Figure 6 : Planar solidification observed in specimen 2. (a) Superimposition of orientation map and BSE-SEM observations showing epitaxy between two dendrites colonies with a  $90^\circ$  rotation, separated by a planar front (dotted lines). (b) Planar-dendritic transition at a melt pool boundary.

## 2.2 Chemical heterogeneities

Table 3 shows the mean composition of the analyzed area for each specimen as measured by averaging all 208 EDS datapoints. Very good agreement is found with EPMA measurements (Table 2), indicating that datasets are representative of the materials. On the other hand, this does not mean that variations within datasets, i.e. chemical heterogeneities, are representative of the whole specimens.

Figure 7 shows the experimentally reconstructed dendritic concentration profiles for chromium, nickel and molybdenum. For clarity, only the mean concentration values at nondimensional length intervals of 0.02 are presented. Molybdenum exhibits the highest redistribution from the core to the interdendritic areas, followed by chromium, while the concentration gradient for nickel is very low. This is in good agreement with the relative values of equilibrium partition coefficients  $k_e$  of these solutes for the liquid/austenite system [9,56,57] and thus to solidification-induced solute redistribution. Based on the compositions reported in Table 2, absolute interdendritic enrichments in chromium, nickel and molybdenum with respect to the core are of about 1-2 wt%, 0.5-1 wt% and 1-1.5 wt%, respectively. This in good agreement with the reported compositions of dendrite cores and boundaries for 316L processed by L-PBF [24,30–34].

Table 3: Average compositions in weight percent as determined by STEM-EDS

	Si	Cr	Mn	Fe	Ni	Mo
Sample 1	0.8	17.2	0.8	65.8	12.8	2.8
Sample 2	0.6	17.9	1.1	65.3	12.9	2.6
Sample 3	0.6	18.1	1.3	65.3	12.2	2.5

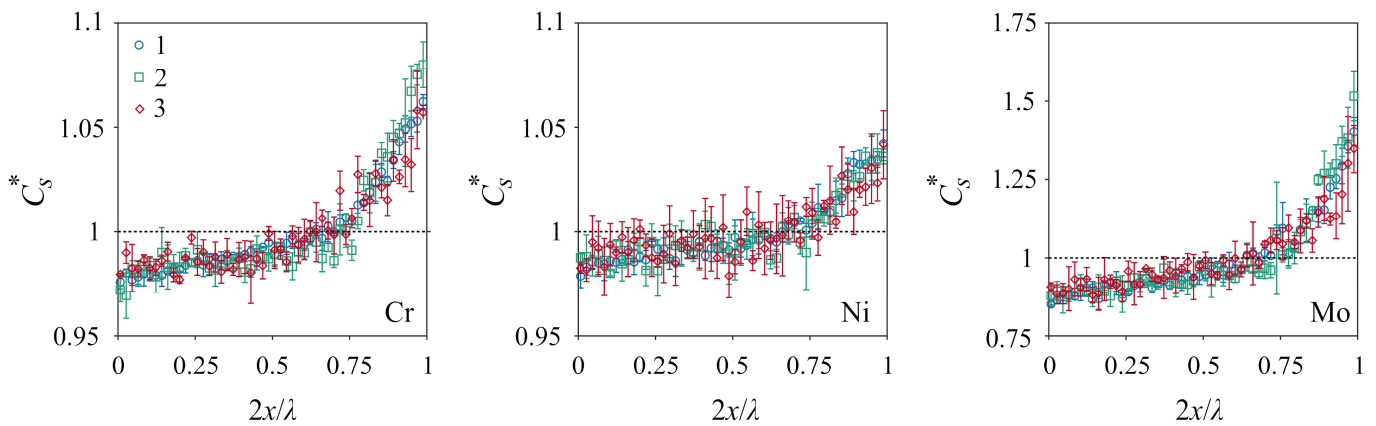


Figure 7: Chromium, nickel and molybdenum nondimensional segregation profiles for the three studied specimen. Markers represent mean concentrations at nondimensional length intervals of 0.02. Mean standard deviations are shown on the left side.

Microsegregation profiles are susceptible to evolve once solidification is complete by solid-state diffusion due to re-heating and cooling cycles stemming from the consolidation of subsequent layers. Figure 8 shows the composition profiles after a cooling from 1300°C to room temperature as calculated with DICTRA. Cooling rate was set to  $10^5 \text{ K.s}^{-1}$ , a very conservative value considering the solidification cooling rates reported in section 2.1. Other hypotheses and parameters used for these calculations are given in section 1.4. While faster homogenization occurs for lower values of  $\lambda$  due to the sharper local gradients of chemical potential and smaller system length, solid-state diffusion mainly affects the interdendritic areas and has an overall weak effect on the composition profiles. As such, the composition profiles from Figure 7 can be considered as representative of the solidification-induced solute segregation, at least for nondimensional lengths up to 0.9.

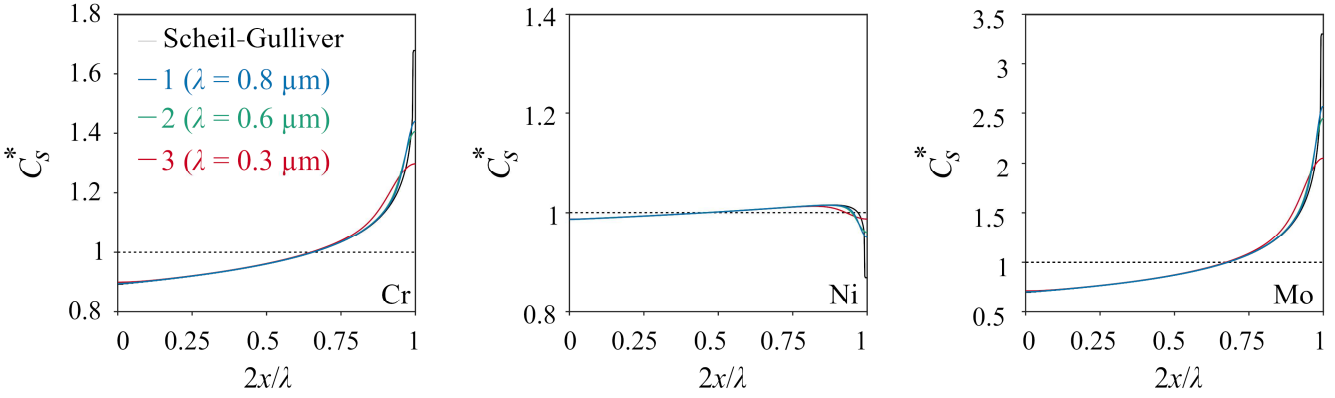


Figure 8: Equilibrium Scheil-Gulliver (S-G) and subsequent concentration profiles after solid-state diffusion during a cooling at  $10^5 \text{ K.s}^{-1}$  for different dendrite diameters

Thus, despite being built with very different parameters and exhibiting different cooling rates, similar composition profiles were measured in all specimens. Furthermore, the cell core and interdendritic compositions determined in this work are in the same order of magnitude than those reported for a wide range of processing conditions, e.g. by Liu et al. (200 W – 850 mm/s) [31], Dépinoy et al. (60 W – 30 mm/s) [9] and Miettinen [56], the latter for welding experiments with an estimated solidification rate of 15 mm/s. It therefore appears that microsegregations in 316L stainless steels processed by L-PBF show little dependency to the processing conditions. Further discussions would require the determination of the solidification rate  $V$ , commonly obtained numerically with the equation  $V = V_b \cos \theta$ , where  $\theta$  is the angle

between the normal to the melt boundary and the scanning direction [13]. For fast scanning speeds, precise determination of  $\theta$  is paramount as deviations of several degrees can strongly affect the value of  $V$ . Since complex phenomena such as Marangoni convection and recoil pressure due to evaporation can have a strong effect on the melt pool shape [58], this requires highly detailed simulations that are outside of the scope of this study.

First insights can nevertheless be inferred from general considerations. It can be deduced from Figure 1 and 5 that the area analyzed by STEM-EDS for specimen 3 is located at the centerline of a molten pool. At this particular location, grains are oriented close to the  $\langle 001 \rangle$  direction with respect to the building direction throughout the melt pool depth. This implies a relatively low solidification rate as  $\theta$  is close to  $90^\circ$ , consistently with the elongated melt pool resulting from fast scanning speeds [59]. As a mean of illustration, Grange et al. [60] numerically determined the melt pool shapes at the centerline for Inconel 738 processed by L-PBF using a highly detailed continuous-mesoscale finite element model. Analysis of their results obtained with a set of parameters almost identical to the one used for building specimen 3 ( $P = 180$  W,  $v = 750$  mm/s,  $\phi = 100$   $\mu$ m) shows that  $\theta$  ranges from  $90^\circ$  to  $85^\circ$  in the bottom half of the melt pool, i.e. a maximum solidification rate of 65 mm/s. While these results are not directly transposable to 316L stainless steels, it nevertheless shows that  $V$  can be an order of magnitude lower than  $V_b$ . Due to the less regular texture of specimens 2 and 3 (Figure 1), it is not possible to assess the locations of EDS analyses within the melt pool, but  $\theta$  is nonetheless expected to be lower as the melt pool shape becomes elliptical with decreasing scan speed [59]. There is therefore the possibility that solidification rates remain within a single decade, i.e. between 10 mm/s and 100 mm/s, regardless of the processing conditions used in this study. No significant solute trapping is expected to occur at these speeds, the characteristic solute trapping velocity being commonly considered to be in the range of 1000 mm/s [61] and the equilibrium coefficients for chromium, nickel and molybdenum being already close to 1. It has further been reported that the dendrite core composition in chromium and molybdenum in 316L is weakly dependent on the solidification rate for  $V > 10$  mm/s, i.e. it varies below the STEM-EDS precision [56]. Similarly, phase field modeling for a simplified austenitic Fe-Cr system [62,63] show that increasing the solidification rate from 12 mm/s to 60 mm/s have a relatively small effect on the chromium segregation.

## 2.4 Dislocations structures

Figure 9 shows typical dislocations structures observed by TEM. Besides the commonly reported interdendritic dense dislocations walls, intradendritic dislocation tangles and cells are observed in agreement with [9,25]. Intradendritic dislocations density is furthermore found to increase with increasing dendrite diameter. Since the dense interdendritic dislocations walls do not correlate with significant crystalline misorientations (section 2.1), they do not consist of geometrically necessary dislocations (GNDs). It follows that dislocations densities in 316L processed by L-PBF cannot be assessed by means of EBSD analyses. These findings thus tend to confirm the thermomechanical origin of dislocations.

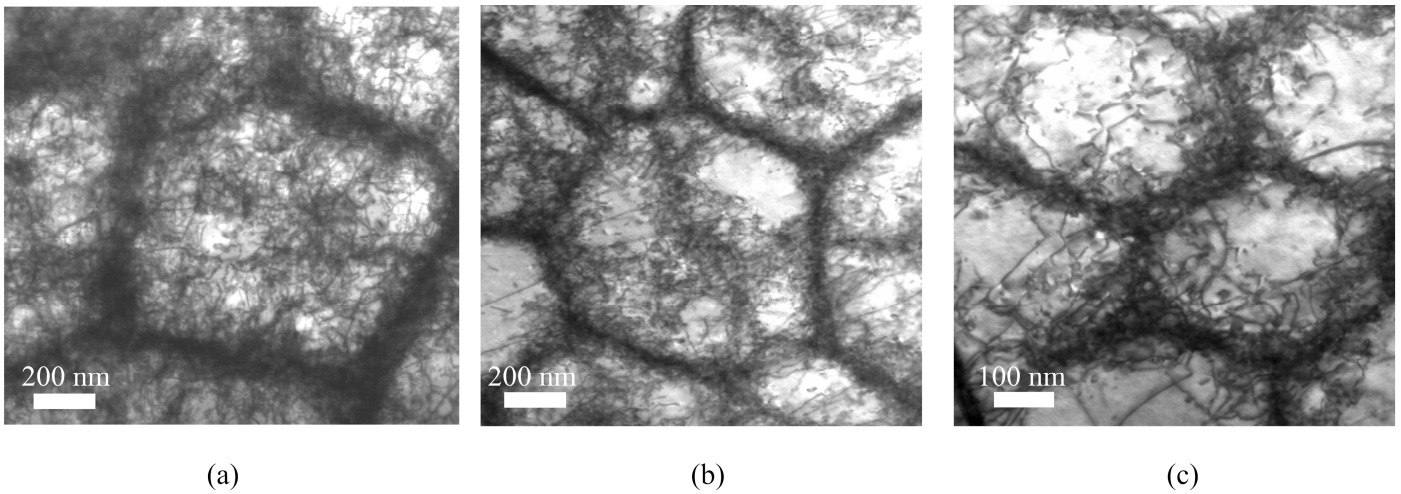


Figure 9: Bright-field STEM observations showing dislocations structures for (a) specimen 1, (b) specimen 2 and (c) specimen 3.

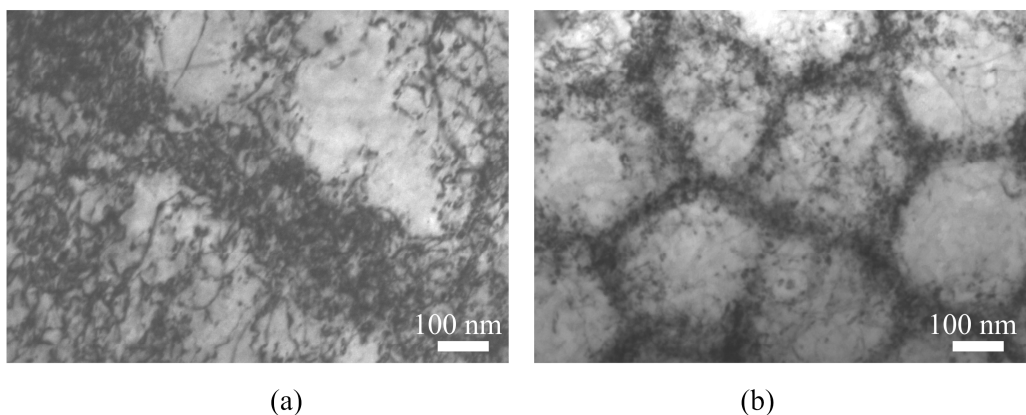


Figure 10: Bright-field TEM observations showing interdendritic dislocations walls for (a) specimen 1, (b) specimen 3.

It is known that mechanical straining leads to the self-organization of dislocations as cells which diameters  $c$  depend on the total dislocations density [64]. Bertsch et al. concluded that the similarity between  $c$  and  $\lambda$  for L-PBF-processed materials resulted in the natural organization of dislocations at interdendritic boundaries [25]. While self-organized dislocations cells are reported during rapid solidification of high-purity copper [21] and slowly grown pure semiconductor crystals [65], it can be argued this mechanism alone is not responsible for dislocation patterning in rapidly solidified alloys. Indeed, there is a clear difference in the organization of interdendritic and intradendritic dislocations between the different specimens, indicating a preferential localization of dislocations at interdendritic boundaries. Furthermore, Figure 10 shows that the thickness of interdendritic dislocations walls is found to scale with the dendrite diameter. A similar observation can be made on STEM images of [25]. These thicknesses appear to be of a similar order of magnitude compared to the chemically enriched interdendritic boundaries thicknesses measured by SEM, implying a strong correlation between the formation of dislocations walls and a critical chemical composition. While this critical composition cannot be conclusively determined due to the uncertainties associated with the interdendritic solute contents, the slightly different average compositions of the specimens would suggest that it is not an absolute one but rather a relative one with respect to the dendrite core composition. Based on these observations, it can be proposed that chemically enriched interdendritic areas act as obstacles to dislocations motion during post-solidification cooling, resulting in the formation of dense interdendritic dislocations walls. This could be related, for instance, to local increase in yield strength [66] and/or decrease of stacking fault energy [67]. Such mechanism would be consistent with the observed correlation between  $\lambda$  and the relative amount of intradendritic dislocations: increasing  $\lambda$  implies that dislocations have to move over a longer mean distance in order to interact with interdendritic boundaries, and consequently that more dislocations remain in the dendrite interior. The extreme case where  $\lambda \gg c$  would further lead to the formation of intradendritic dislocations cells of the kind observed by [9,25] for large values of  $\lambda$ .

This theory is further backed by several observations from the literature. Recent dislocation dynamics simulations performed by Sudmanns et al. shows that dislocation slip is interrupted at interdendritic areas due to compositional fluctuations [68]. Furthermore, the very good thermal and mechanical stability of interdendritic dislocations is often attributed to a pinning effect related to the local solute enrichment

[24,31,32,69], and Voisin et al. noticed a higher density of stacking faults in interdendritic areas, implying a higher density of sessile dislocations compared to the dendrite interior [24]. Finally, crystal plasticity calculations showed that variations of solute enrichment led to strain partitioning at the dendrite scale during post-solidification cooling, with a preferential deformation of the dendrite core but not of the interdendritic boundaries [62]. While the authors concluded that dendrites cores contained more dislocations, one can argue that the motion of these dislocations would be ultimately hindered at the harder interdendritic boundaries.

Thus, providing that thermomechanical stresses are large enough to induce sufficient plastic straining during the process, current results suggest that dislocations patterning is solely controlled by the amplitude and the wavelength of chemical fluctuations. In the particular framework of this study, where no strong dependency of interdendritic solute enrichment on the solidification conditions has been found, the main parameter affecting dislocation patterning thus appears to be the cooling rate during solidification through its effect on the interdendritic spacing.

## **2.4 Mechanical properties**

Figure 11 shows the true stress-true strain compression curves for the three specimens. Yield strengths in compression for specimen 1, 2 and 3 are respectively in the range of 555-565 MPa, 540-550 MPa and 565-570 MPa. No direct correlation between the yield strength and the process parameters is thus observed. Note that, on the other hand, strain-hardening at the onset of plasticity appears to be condition-dependent.

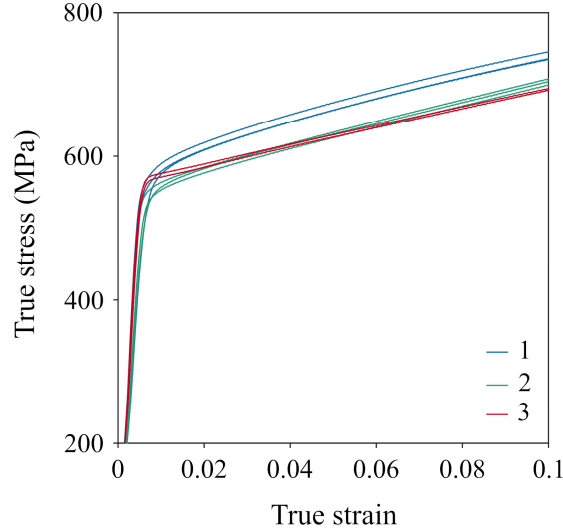


Figure 11: Compression true stress-true strain curves

Since all other factors affecting the yield strength can be assumed constant (i.e. crystalline texture and grain size in the compression axis, see Figure 1b), it can be concluded that variations in the substructure organization has a marginal effect on the yield strength. While this is rather surprising considering the significant differences between specimens, similar observations of different dendrite sizes resulting in almost identical yield strengths are reported in the literature [70,71]. Current results thus unambiguously show that the yield strength dependency on the substructure can be more complex than a simple Hall-Petch-like effect of the dendrite size  $\lambda$ . Based on the previous microstructural characterizations, this can be explained by two factors. First, contrarily to conventional Hall-Petch mechanism which involves high-angle boundaries, dendrites are only weakly misoriented with respect to each other (section 2.2). In this case, strengthening arises from the segregation-stabilized interdendritic dislocations walls that act as soft barriers, hindering the dislocations motion [22,31]. It can therefore be argued that the substructure-induced strengthening is a function of the thickness of these interdendritic dislocations walls, and thus may vary between the different specimens. Second, the characteristic length of such Hall-Petch-like mechanism is the mean-free path of mobile dislocations, i.e. the projected dendrite size on the  $\{111\}$  slip planes [24,55]. In this study, coarser dendrites result in a higher intradendritic dislocations density, thus any softening related to the increase of this mean-free path implies a higher dislocations strengthening. The similar yield strength exhibited by the different specimens may therefore be the result of different strengthening mechanisms

depending on the organization of the intragranular substructure. On the other hand, these different organizations, among other factors, may be linked to differences in strain-hardening behavior.

## **Conclusion**

The effect of solidification conditions on the fine-scale microstructural features of 316L built by L-PBF was investigated. Solute redistribution profiles were found to be consistent with primary austenitic solidification. Similar amplitudes of microsegregations were observed regardless of the processing conditions. This can be attributed to the fact that large variations of scanning speeds result in comparatively small variations of solidification rates, with an overall weak effect of the final solute redistribution behavior. Further work is however needed to confirm this theory, for instance by duplicating this study on TEM samples taken at different locations from a single melt pool, thus corresponding to different solidification rates. Very small misorientations were found between dendrites, indicating that dislocations are not GNDs in nature but originate from thermomechanical stresses, and no evidences of *in-situ* recovery or recrystallization were observed. Dislocations patterning was found to be strongly correlated to the periodicity of chemical fluctuations, such that larger interdendritic spacing resulted in thicker interdendritic dislocation walls and higher intradendritic dislocations density. This would suggest that dislocations motion resulting from thermomechanical plastic straining is impeded at the solute-enriched interdendritic boundaries. As such, providing that thermomechanical stresses are large enough to induce sufficient plastic straining, dislocations structures are believed to be primarily controlled by (i) the cooling rate during solidification due to its effect on the interdendritic spacing and (ii) the solidification rate which governs the amplitude of microsegregations. In the particular case of 316L, microsegregations were found to remain similar regardless of the processing conditions and dislocations patterns thus appear to be mainly controlled by the dendrite size. Finally, no simple Hall-Petch-like relationship was found between the dendrite size and the yield strength for the studied specimens. This may be related to different strengthening mechanisms depending on the dislocations patterning.

Current results are thus a first step for controlling the final properties of 316L built by L-PBF by fine-tuning the intragranular substructure through the choice of processing conditions. Strain-hardening appear to be affected by the dislocations structures, and thus by the interdendritic spacing, and the similar

amplitude, but different wavelengths of microsegregations, obtained by different sets of parameters are likely to impact the resistance against corrosion. Subsequent studies focusing on these last two points are ongoing.

### **Acknowledgements**

The author would like to thank Lyliat Ferhat, Jean-Christophe Teissedre, Mohamed Sennour and Lynh-Thy Tran-Hoang for their help with the L-PBF process, compression tests, TEM observations and EPMA analyses, respectively.

## Appendix: Assessment of the reliability of STEM-EDS measurements

Quantitative EDS measurements rely on the Cliff-Lorimer equation:

$$\frac{C_i}{C_j} = K_{ij} \frac{I_i}{I_j} \tag{A1}$$
$$\sum_1^N C_i = 100 \%$$

where  $C_i$  and  $I_i$  are respectively the weight percentage and the peak intensity of element  $i$ , subscript  $j$  denotes the reference element,  $N$  is the total number of considered elements and  $K$  is the Cliff-Lorimer factor, a parameter function of the atomic number, of the accelerating voltage and of the detector configuration. Precise determination of the composition thus relies on precise peak intensities and Cliff-Lorimer factors. These two points are discussed in the following along with the spatial resolution of the measurements.

### Measurements dependence on Cliff-Lorimer factors

In this study, STEM-EDS quantifications were achieved using standardless Cliff-Lorimer factors supplied by the detector manufacturer, a reasonable but potentially inaccurate approximation of the true Cliff-Lorimer factors. Moreover, analyses were performed on thin foils with unknown and potentially irregular thicknesses, which can induce further bias. Indeed, equation (A1) is rigorously valid for zero-thickness specimens: the thicker the specimen, the likelier X-Rays absorption can occur. This implies that the amount of X-Rays detected is less than the X-Rays generated from specimen, breaking the proportionality of  $C_i$  to  $I_i$ . Thus, the validity of the EDS quantifications as performed in this study must be thoroughly discussed. To this end, a numerical evaluation of the effect of the Cliff-Lorimer factors on the final results has been conducted.

A set of 200 composition points including silicon, chromium, manganese, iron, nickel and molybdenum were randomly generated with a maximal relative deviation of  $\pm 25\%$  from the nominal

powder composition (Table 2). Iron was taken as the balance element. X-Rays absorption can be taken into account in an effective Cliff-Lorimer factor,  $K_{ij}^c$ , written as [72]:

$$K_{ij}^c = K_{ij} \left( \frac{\left( \frac{\mu}{\rho} \right)_{spec}^i}{\left( \frac{\mu}{\rho} \right)_{spec}^j} \right) \left( \frac{1 - e^{-\left( \frac{\mu}{\rho} \right)_{spec}^j \rho t \cos \alpha}}{1 - e^{-\left( \frac{\mu}{\rho} \right)_{spec}^i \rho t \cos \alpha}} \right) \quad (A2)$$

where  $\left( \frac{\mu}{\rho} \right)_{spec}^i$  is the mass-absorption coefficient of X-rays from element  $i$  in the specimen [72], gathered from [73],  $\rho$  is the specimen density (8000 kg/m<sup>3</sup> for stainless steel),  $t$  is the specimen thickness and  $\alpha$  is the take-off angle. Effective Cliff-Lorimer factors for each datapoint were calculated using Equation (A2) for thicknesses up to 400 nm. Misestimated concentrations  $C_i^*$  were then recalculated assuming an effective Cliff-Lorimer factor  $K_{ij}^{c*}$  corresponding to a thickness of 100 nm.

It is found that misestimating the specimen thickness mostly affects the silicon concentration with a relative error of up to 50%, while the relative errors for other elements are less than 5% (Figure A1a). This is related to the lower mass-absorption coefficients for heavier elements. However, relative errors between true and misestimated concentrations can be further reduced to less than 2%, regardless of the element of interest, by considering the nondimensional concentrations  $C_i/\bar{C}_i$  and  $C_i^*/\bar{C}_i^*$ , where the overline denotes the average concentration (Figure A1b). In other words, this means that the deviation from the average concentration is only lightly affected by the choice of the specimen thickness, i.e. the Cliff-Lorimer factors. In fact, these observations hold true even if the Cliff-Lorimer factors are randomly chosen between 75% and 125% of their value. Thus, normalizing by the average concentration negates a large part of the error carried by the Cliff-Lorimer factors.

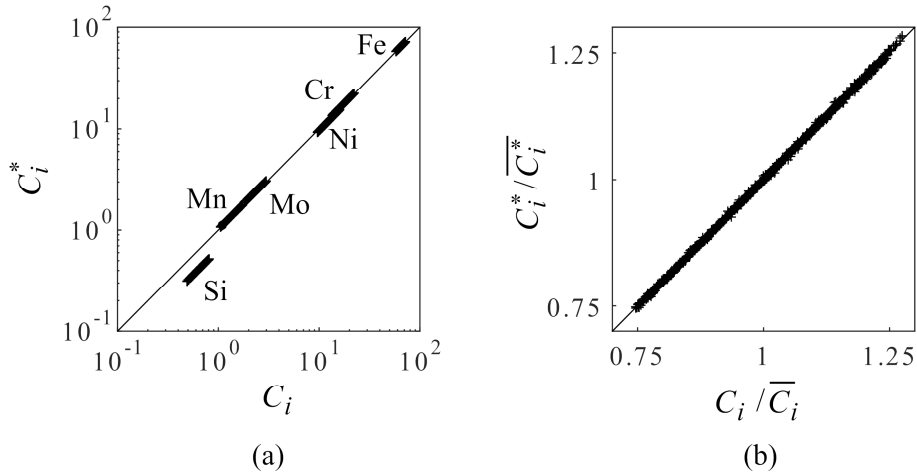


Figure A1: Misestimated concentrations as a function of the true concentrations for the extreme case of  $t = 400$  nm: (a) absolute values, (b) normalized values.

Further calculations were performed considering a specimen of uneven thickness ranging from 50 nm to 250 nm with a step of 50 nm. As shown in Figure A2, not accounting for the variation of thickness leads to nondimensional concentrations misestimated by less than 2% for every element with the notable exception of silicon. Thus, this element is included in the quantification scheme but its variation is not discussed. Note that any increase in the steepness of the thickness gradient would increase this systematic error.

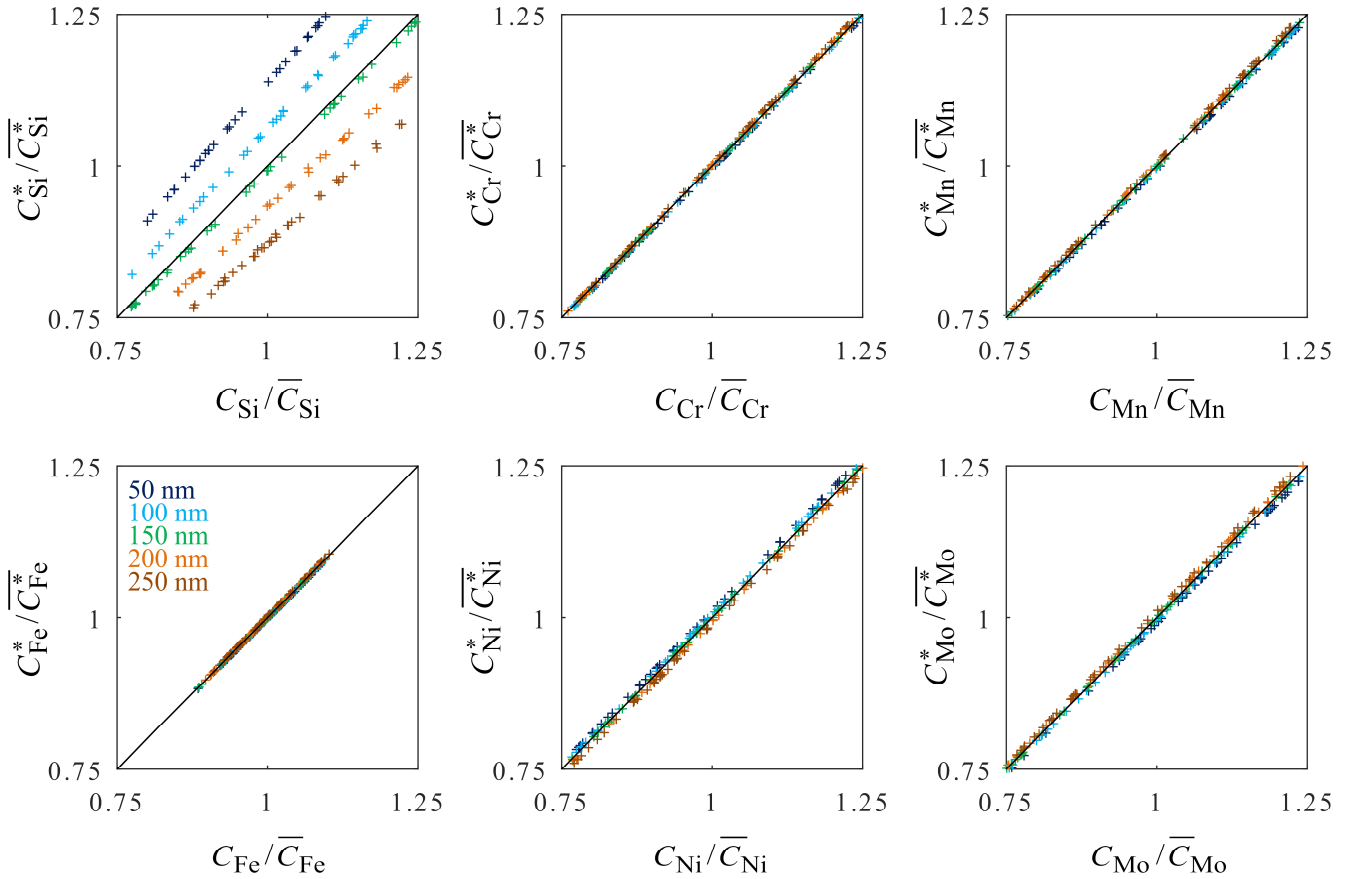


Figure A2: Nondimensional misestimated concentrations as a function of the nondimensional true concentrations for every element, assuming a specimen with uneven thickness ranging from 50 nm to 250 nm with a step of 50 nm.

### Measurements dependence on the peak intensities

Peak intensities depend on the counting statistics, i.e. the number of X-Rays that are counted by the detector, and by the post-processing scheme. In this study, the post-processing scheme was performed with the Esprit 2.2 software as followed. The background was theoretically calculated and subtracted prior to any quantification. Silicon, chromium, manganese, iron, nickel and molybdenum were considered for quantification using their K-lines. Oxygen, sulfur and carbon were used for peak deconvolution but not quantified. Standardless Cliff-Lorimer factors were corrected assuming an arbitrary sample thickness of 100 nm together with a material density of 8000 kg/m<sup>3</sup>.

A depleted cell core and an enriched interdendritic region were probed five times in Specimen 3 to assess the variation of peak intensities. Results are shown in Table A1. It appears that variations in concentration are in the same order of magnitude that variations of the peak intensity. There are thus higher

uncertainties for lower concentrations: this can be seen for minor elements such as silicon, manganese and molybdenum, but also appears clearly when comparing the enriched region with the depleted one. Analyses of the spectra further showed that manganese was subjected to noisy variations within a specimen. This is related to the pathological overlap of the  $K_{\beta}$  and  $K_{\alpha}$  lines of Cr/Mn and Mn/Fe in conjunction of the very low relative amount of manganese with respect to iron and chromium.

*Table A1: Relative deviations of the peak intensity and of the absolute concentration (in wt%) for five measurements on a given spot.*

Deviation from mean value (%)	Si	Cr	Mn	Fe	Ni	Mo
Interdendritic (enriched)						
Net counts	2.1	0.4	2.7	0.1	0.2	1.7
Concentration	2.0	0.3	2.7	< 0.1	0.3	1.5
Core (depleted)						
Net counts	2.1	0.5	3.5	0.1	0.7	2.8
Concentration	2.0	0.4	4.0	0.2	0.6	2.6

### **Comparison between the theoretical and the experimental errors**

Based on these considerations, the following guidelines have been used for the EDS quantification. Results are presented as nondimensional concentrations to reduce the error related of the choice of the Cliff-Lorimer factors. Silicon and manganese elements were included in the quantification but their trend is not discussed due to their large relative errors stemming from the Cliff-Lorimer factors and of their intensities, respectively. It is assumed that any error in these minor elements have a negligible effect on the concentration of other elements. The maximum relative error for chromium, nickel, iron and molybdenum concentrations are taken as the sum of the maximum errors stemming from the Cliff-Lorimer factors (taken as 2%) and the peak intensities. The experimental error has been determined as the average standard deviations at nondimensional length intervals of 0.02. Comparison between theoretical and experimental errors is shown in Table A2. Experimental errors are always lower or in the same range as the maximum estimated theoretical error.

*Table A2: Comparison between the maximum theoretical error and the experimental ones.*

Relative error (%)	Cr	Fe	Ni	Mo
Theoretical maximum	3	2	3	5
Sample 1	0.6	0.1	0.9	4.2
Sample 2	0.6	0.1	0.7	3.3
Sample 3	0.6	0.1	0.6	2.8

Final validation of the experimental measurements relies on two points. First, since a nondimensional concentration implies a division by the average concentration, the latter must be representative of the material. Based on the comparison of Tables 2 and 3, this condition is fulfilled in the present study. Second, the observed variations in nondimensional concentrations must be higher than any systematic error, taken here as the theoretical maximum error. It is found that the full range of concentration variations is always higher than this limit by a factor ranging from 2 to 10. Thus, it can be concluded that EDS measurements are representative of the specimen, and that measured variations are due to gradients in chemical composition within a specimen.

### **Spatial resolution of EDS measurements**

EDS analyses were not performed exactly edge-on but with a slight misorientation of typically  $5^\circ$  between the incident beam and the  $\langle 001 \rangle$  zone axis. For a typical thin foil thickness of 100 nm, and assuming a constant amount of X-Rays generated over the thickness, this implies that each EDS measurement corresponds to the average composition of  $\sim 8$  nm in width. By considering the typical dendrite radii for each specimen, this length corresponds to an average nondimensional length of 0.02, 0.03 and 0.05 for specimen 1 to 3, respectively. This uncertainty is considered to be acceptable within the framework of the current study.

### **References**

- [1] K. Saeidi, X. Gao, Y. Zhong, Z.J. Shen, Hardened austenite steel with columnar sub-grain structure formed by laser melting, *Mater. Sci. Eng. A.* 625 (2015) 221–229. <https://doi.org/10.1016/j.msea.2014.12.018>.
- [2] A. Hadadzadeh, B. Shalchi Amirkhiz, A. Odeshi, J. Li, M. Mohammadi, Role of hierarchical microstructure of additively manufactured AlSi10Mg on dynamic loading behavior, *Addit. Manuf.* 28 (2019) 1–13. <https://doi.org/10.1016/j.addma.2019.04.012>.
- [3] W.M. Tucho, P. Cuvillier, A. Sjolyst-Kverneland, V. Hansen, Microstructure and hardness studies of Inconel 718 manufactured by selective laser melting before and after solution heat treatment, *Mater. Sci. Eng. A.* 689 (2017) 220–232. <https://doi.org/10.1016/j.msea.2017.02.062>.

- [4] Z.G. Zhu, Q.B. Nguyen, F.L. Ng, X.H. An, X.Z. Liao, P.K. Liaw, S.M.L. Nai, J. Wei, Hierarchical microstructure and strengthening mechanisms of a CoCrFeNiMn high entropy alloy additively manufactured by selective laser melting, *Scr. Mater.* 154 (2018) 20–24. <https://doi.org/10.1016/j.scriptamat.2018.05.015>.
- [5] D. Kong, C. Dong, S. Wei, X. Ni, L. Zhang, R. Li, L. Wang, C. Man, X. Li, About metastable cellular structure in additively manufactured austenitic stainless steels, *Addit. Manuf.* 38 (2021) 101804. <https://doi.org/10.1016/j.addma.2020.101804>.
- [6] W. Kurz, D. Fischer, *Fundamentals of Solidification*, 1998. <https://doi.org/10.31399/asm.hb.v09.a0003724>.
- [7] S. Katayama, A. Matsunawa, Solidification microstructure of laser welded stainless steels, in: *Int. Congr. Appl. Lasers Electro-Optics*, Laser Institute of America, 1984: pp. 60–67. <https://doi.org/10.2351/1.5057623>.
- [8] U. Scipioni Bertoli, B.E. MacDonald, J.M. Schoenung, Stability of cellular microstructure in laser powder bed fusion of 316L stainless steel, *Mater. Sci. Eng. A.* 739 (2019) 109–117. <https://doi.org/10.1016/J.MSEA.2018.10.051>.
- [9] S. Dépinoy, M. Sennour, L. Ferhat, C. Colin, Experimental determination of solute redistribution behavior during solidification of additively manufactured 316L, *Scr. Mater.* 194 (2021) 113663. <https://doi.org/10.1016/j.scriptamat.2020.113663>.
- [10] J.W. Elmer, S.M. Allen, T.W. Eagar, Microstructural development during solidification of stainless steel alloys, *Metall. Trans. A.* 20 (1989) 2117–2131. <https://doi.org/10.1007/BF02650298>.
- [11] N. Suutala, Effect of solidification conditions on the solidification mode in austenitic stainless steels, *Metall. Trans. A.* 14 (1983) 191–197. <https://doi.org/10.1007/BF02651615>.
- [12] S. Fukumoto, W. Kurz, Solidification Phase and Microstructure Selection Maps for Fe-Cr-Ni Alloys., *ISIJ Int.* 39 (1999) 1270–1279. <https://doi.org/10.2355/isijinternational.39.1270>.
- [13] M. Rappaz, S.A. David, J.M. Vitek, L.A. Boatner, Development of microstructures in Fe-15Ni-15Cr single crystal electron beam welds, *Metall. Trans. A.* 20 (1989) 1125–1138. <https://doi.org/10.1007/BF02650147>.
- [14] X. Tong, C. Beckermann, A diffusion boundary layer model of microsegregation, *J. Cryst. Growth.*

187 (1998) 289–302. [https://doi.org/10.1016/S0022-0248\(97\)00878-6](https://doi.org/10.1016/S0022-0248(97)00878-6).

- [15] R. Trivedi, W. Kurz, Dendritic growth, *Int. Mater. Rev.* 39 (1994) 49–74. <https://doi.org/10.1179/imr.1994.39.2.49>.
- [16] M.J. Aziz, T. Kaplan, Continuous growth model for interface motion during alloy solidification, *Acta Metall.* 36 (1988) 2335–2347. [https://doi.org/10.1016/0001-6160\(88\)90333-1](https://doi.org/10.1016/0001-6160(88)90333-1).
- [17] M.J. Aziz, W.J. Boettinger, On the transition from short-range diffusion-limited to collision-limited growth in alloy solidification, *Acta Metall. Mater.* 42 (1994) 527–537. [https://doi.org/10.1016/0956-7151\(94\)90507-X](https://doi.org/10.1016/0956-7151(94)90507-X).
- [18] T. Billotte, D. Daloz, B. Rouat, G. Tirand, J. Kennedy, V. Robin, J. Zollinger, Microsegregation Model Including Convection and Tip Undercooling: Application to Directional Solidification and Welding, *Materials (Basel)*. 11 (2018) 1252. <https://doi.org/10.3390/ma11071252>.
- [19] R. Ananth, W.N. Gill, Self-consistent theory of dendritic growth with convection, *J. Cryst. Growth*. 108 (1991) 173–189. [https://doi.org/10.1016/0022-0248\(91\)90365-C](https://doi.org/10.1016/0022-0248(91)90365-C).
- [20] Z. Zhu, W. Li, Q.B. Nguyen, X. An, W. Lu, Z. Li, F.L. Ng, S.M. Ling Nai, J. Wei, Enhanced strength–ductility synergy and transformation-induced plasticity of the selective laser melting fabricated 304L stainless steel, *Addit. Manuf.* 35 (2020) 101300. <https://doi.org/10.1016/j.addma.2020.101300>.
- [21] G. Wang, H. Ouyang, C. Fan, Q. Guo, Z. Li, W. Yan, Z. Li, The origin of high-density dislocations in additively manufactured metals, *Mater. Res. Lett.* 8 (2020) 283–290. <https://doi.org/10.1080/21663831.2020.1751739>.
- [22] Y.M. Wang, T. Voisin, J.T. McKeown, J. Ye, N.P. Calta, Z. Li, Z. Zeng, Y. Zhang, W. Chen, T.T. Roehling, R.T. Ott, M.K. Santala, P.J. Depond, M.J. Matthews, A. V. Hamza, T. Zhu, Additively manufactured hierarchical stainless steels with high strength and ductility, *Nat. Mater.* 17 (2018) 63–71. <https://doi.org/10.1038/nmat5021>.
- [23] J.R. Foulds, J. Moteff, Substructure Characterization of a 16-8-2 GTA weld through transmission electron microscopy, *Weld. J. Res. Suppl.* 61 (1982) 189S-196S.
- [24] T. Voisin, J.B. Forien, A. Perron, S. Aubry, N. Bertin, A. Samanta, A. Baker, Y.M. Wang, New insights on cellular structures strengthening mechanisms and thermal stability of an austenitic

- stainless steel fabricated by laser powder-bed-fusion, *Acta Mater.* 203 (2021) 116476. <https://doi.org/10.1016/j.actamat.2020.11.018>.
- [25] K.M. Bertsch, G. Meric de Bellefon, B. Kuehl, D.J. Thoma, Origin of dislocation structures in an additively manufactured austenitic stainless steel 316L, *Acta Mater.* 199 (2020) 19–33. <https://doi.org/10.1016/j.actamat.2020.07.063>.
- [26] S. Chen, G. Ma, G. Wu, A. Godfrey, T. Hang, X. Huang, Strengthening mechanisms in selective laser melted 316L stainless steel, *Mater. Sci. Eng. A.* (2021) 142434. <https://doi.org/10.1016/J.MSEA.2021.142434>.
- [27] T. Vilaro, C. Colin, J.D. Bartout, L. Nazé, M. Sennour, Microstructural and mechanical approaches of the selective laser melting process applied to a nickel-base superalloy, *Mater. Sci. Eng. A.* 534 (2012) 446–451. <https://doi.org/10.1016/J.MSEA.2011.11.092>.
- [28] A.J. Birnbaum, J.C. Steuben, E.J. Barrick, A.P. Iliopoulos, J.G. Michopoulos, Intrinsic strain aging,  $\Sigma$ 3 boundaries, and origins of cellular substructure in additively manufactured 316L, *Addit. Manuf.* 29 (2019) 100784. <https://doi.org/10.1016/j.addma.2019.100784>.
- [29] P. Krakhmalev, I. Yadroitsava, G. Fredriksson, I. Yadroitsev, Microstructural and thermal stability of selective laser melted 316L stainless steel single tracks, *South African J. Ind. Eng.* 28 (2017) 12–19. <https://doi.org/10.7166/28-1-1466>.
- [30] M. Godec, S. Zaefferer, B. Podgornik, M. Šinko, E. Tchernychova, Quantitative multiscale correlative microstructure analysis of additive manufacturing of stainless steel 316L processed by selective laser melting, *Mater. Charact.* 160 (2020) 110074. <https://doi.org/10.1016/j.matchar.2019.110074>.
- [31] L. Liu, Q. Ding, Y. Zhong, J. Zou, J. Wu, Y.-L.L. Chiu, J. Li, Z. Zhang, Q. Yu, Z. Shen, Dislocation network in additive manufactured steel breaks strength–ductility trade-off, *Mater. Today.* 21 (2018) 354–361. <https://doi.org/10.1016/J.MATTOD.2017.11.004>.
- [32] H. Yin, M. Song, P. Deng, L. Li, B.C. Prorok, X. Lou, Thermal stability and microstructural evolution of additively manufactured 316L stainless steel by laser powder bed fusion at 500–800 °C, *Addit. Manuf.* 41 (2021) 101981. <https://doi.org/10.1016/j.addma.2021.101981>.
- [33] R.I. Revilla, M. Van Calster, M. Raes, G. Arroud, F. Andreatta, L. Pyl, P. Guillaume, I. De Graeve,

Microstructure and corrosion behavior of 316L stainless steel prepared using different additive manufacturing methods: A comparative study bringing insights into the impact of microstructure on their passivity, *Corros. Sci.* 176 (2020) 108914. <https://doi.org/10.1016/j.corsci.2020.108914>.

- [34] D. Kong, C. Dong, X. Ni, L. Zhang, H. Luo, R. Li, L. Wang, C. Man, X. Li, The passivity of selective laser melted 316L stainless steel, *Appl. Surf. Sci.* 504 (2020) 144495. <https://doi.org/10.1016/j.apsusc.2019.144495>.
- [35] Y. Zhong, L. Liu, S. Wikman, D. Cui, Z. Shen, Intragranular cellular segregation network structure strengthening 316L stainless steel prepared by selective laser melting, *J. Nucl. Mater.* 470 (2016) 170–178. <https://doi.org/10.1016/j.jnucmat.2015.12.034>.
- [36] M. Wang, M.H. Fan, S. Cruchley, Y.L. Chiu, Effect of cellular dislocation structure on the strength of additively manufactured 316L stainless steel, in: *Mater. Sci. Forum*, Trans Tech Publications Ltd, 2021: pp. 1576–1584. <https://doi.org/10.4028/www.scientific.net/MSF.1016.1576>.
- [37] S. Gorsse, C. Hutchinson, M. Gouné, R. Banerjee, Additive manufacturing of metals: a brief review of the characteristic microstructures and properties of steels, Ti-6Al-4V and high-entropy alloys, *Sci. Technol. Adv. Mater.* 18 (2017) 584–610. <https://doi.org/10.1080/14686996.2017.1361305>.
- [38] G. Mohr, S.J. Altenburg, K. Hilgenberg, Effects of inter layer time and build height on resulting properties of 316L stainless steel processed by laser powder bed fusion, *Addit. Manuf.* 32 (2020) 101080. <https://doi.org/10.1016/j.addma.2020.101080>.
- [39] G. Mohr, K. Sommer, T. Knobloch, S.J. Altenburg, S. Recknagel, D. Bettge, K. Hilgenberg, Process Induced Preheating in Laser Powder Bed Fusion Monitored by Thermography and Its Influence on the Microstructure of 316L Stainless Steel Parts, *Metals (Basel)*. 11 (2021) 1063. <https://doi.org/10.3390/met>.
- [40] X. He, T. DebRoy, P.W. Fuerschbach, Alloying element vaporization during laser spot welding of stainless steel, *J. Phys. D. Appl. Phys.* 36 (2003) 3079–3088. <https://doi.org/10.1088/0022-3727/36/23/033>.
- [41] P.A.A. Khan, T. DebRoy, Alloying element vaporization and weld pool temperature during laser welding of AISI 202 stainless steel, *Metall. Trans. B.* 15 (1984) 641–644. <https://doi.org/10.1007/BF02657284>.

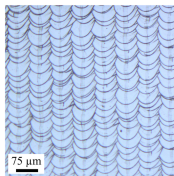
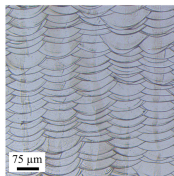
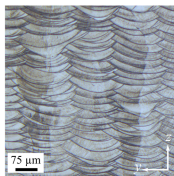
- [42] F. Bachmann, R. Hielscher, H. Schaeben, Texture analysis with MTEX- Free and open source software toolbox, in: *Solid State Phenom.*, Trans Tech Publications Ltd, 2010: pp. 63–68. <https://doi.org/10.4028/www.scientific.net/SSP.160.63>.
- [43] M. Ganesan, D. Dye, P.D. Lee, A technique for characterizing microsegregation in multicomponent alloys and its application to single-crystal superalloy castings, *Metall. Mater. Trans. A Phys. Metall. Mater. Sci.* 36 (2005) 2191–2204. <https://doi.org/10.1007/s11661-005-0338-2>.
- [44] O. Andreau, I. Koutiri, P. Peyre, J.D. Penot, N. Saintier, E. Pessard, T. De Terris, C. Dupuy, T. Baudin, Texture control of 316L parts by modulation of the melt pool morphology in selective laser melting, *J. Mater. Process. Technol.* 264 (2019) 21–31. <https://doi.org/10.1016/j.jmatprotec.2018.08.049>.
- [45] S.-H.H. Sun, T. Ishimoto, K. Hagihara, Y. Tsutsumi, T. Hanawa, T. Nakano, Excellent mechanical and corrosion properties of austenitic stainless steel with a unique crystallographic lamellar microstructure via selective laser melting, *Scr. Mater.* 159 (2019) 89–93. <https://www.sciencedirect.com/science/article/pii/S1359646218305682?via%3Dihub> (accessed January 10, 2020).
- [46] T. Ishimoto, S. Wu, Y. Ito, S.-H. Sun, H. Amano, T. Nakano, Crystallographic Orientation Control of 316L Austenitic Stainless Steel via Selective Laser Melting, *ISIJ Int.* 60 (2020) 1758–1764. <https://doi.org/10.2355/isijinternational.ISIJINT-2019-744>.
- [47] J.J. Marattukalam, D. Karlsson, V. Pacheco, P. Beran, U. Wiklund, U. Jansson, B. Hjärvarsson, M. Sahlberg, The effect of laser scanning strategies on texture, mechanical properties, and site-specific grain orientation in selective laser melted 316L SS, *Mater. Des.* 193 (2020) 108852. <https://doi.org/10.1016/j.matdes.2020.108852>.
- [48] O. Gokcekaya, T. Ishimoto, S. Hibino, J. Yasutomi, T. Narushima, T. Nakano, Unique crystallographic texture formation in Inconel 718 by laser powder bed fusion and its effect on mechanical anisotropy, *Acta Mater.* 212 (2021) 116876. <https://doi.org/10.1016/j.actamat.2021.116876>.
- [49] O. Zinovieva, V. Romanova, R. Balokhonov, Effects of scanning pattern on the grain structure and elastic properties of additively manufactured 316L austenitic stainless steel, *Mater. Sci. Eng. A.*

(2021) 142447. <https://doi.org/10.1016/j.msea.2021.142447>.

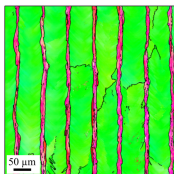
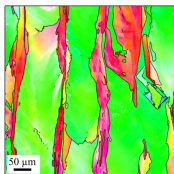
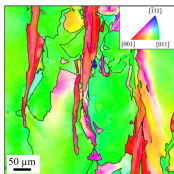
- [50] L. Cui, S. Jiang, J. Xu, R.L. Peng, R.T. Mousavian, J. Moverare, Revealing relationships between microstructure and hardening nature of additively manufactured 316L stainless steel, *Mater. Des.* 198 (2021) 109385. <https://doi.org/10.1016/j.matdes.2020.109385>.
- [51] H.E. Sabzi, E. Hernandez-Nava, X.-H. Li, H. Fu, D. San-Martín, P.E.J. Rivera-Díaz-del-Castillo, Strengthening control in laser powder bed fusion of austenitic stainless steels via grain boundary engineering, *Mater. Des.* 212 (2021) 110246. <https://doi.org/10.1016/j.matdes.2021.110246>.
- [52] N.S. Hussein, D.P. Kumah, J.Z. Yi, C.J. Torbet, D.A. Arms, E.M. Dufresne, T.M. Pollock, J. Wayne Jones, R. Clarke, Mapping single-crystal dendritic microstructure and defects in nickel-base superalloys with synchrotron radiation, *Acta Mater.* 56 (2008) 4715–4723. <https://doi.org/10.1016/j.actamat.2008.05.041>.
- [53] A. Frenk, W. Kurz, Microstructure formation in laser materials processing, *Lasers Eng.* 1 (1992) 193–212.
- [54] M.S. Pham, B. Dovggy, P.A. Hooper, C.M. Gourlay, A. Piglione, The role of side-branching in microstructure development in laser powder-bed fusion, *Nat. Commun.* 11 (2020). <https://doi.org/10.1038/s41467-020-14453-3>.
- [55] D. Wang, C. Song, Y. Yang, Y. Bai, Investigation of crystal growth mechanism during selective laser melting and mechanical property characterization of 316L stainless steel parts, *Mater. Des.* 100 (2016) 291–299. <https://doi.org/10.1016/J.MATDES.2016.03.111>.
- [56] J. Miettinen, Thermodynamic-kinetic simulation of constrained dendrite growth in steels, *Metall. Mater. Trans. B Process Metall. Mater. Process. Sci.* 31 (2000) 365–379. <https://doi.org/10.1007/s11663-000-0055-6>.
- [57] J.A. Brooks, J.C. Williams, A.W. Thompson, STEM Analysis of Primary Austenite Solidified Stainless Steel Welds., *Metall. Trans. A, Phys. Metall. Mater. Sci.* 14 A (1983) 23–31. <https://doi.org/10.1007/BF02643733>.
- [58] Y.H. Siao, C. Da Wen, Examination of molten pool with Marangoni flow and evaporation effect by simulation and experiment in selective laser melting, *Int. Commun. Heat Mass Transf.* 125 (2021) 105325. <https://doi.org/10.1016/j.icheatmasstransfer.2021.105325>.

- [59] T. DebRoy, H.L. Wei, J.S. Zuback, T. Mukherjee, J.W. Elmer, J.O. Milewski, A.M. Beese, A. Wilson-Heid, A. De, W. Zhang, Additive manufacturing of metallic components – Process, structure and properties, *Prog. Mater. Sci.* 92 (2018) 112–224. <https://doi.org/10.1016/j.pmatsci.2017.10.001>.
- [60] D. Grange, A. Queva, G. Guillemot, M. Bellet, J.D. Bartout, C. Colin, Effect of processing parameters during the laser beam melting of Inconel 738: Comparison between simulated and experimental melt pool shape, *J. Mater. Process. Technol.* 289 (2021) 116897. <https://doi.org/10.1016/j.jmatprotec.2020.116897>.
- [61] M.J. Aziz, Interface attachment kinetics in alloy solidification, *Metall. Mater. Trans. A Phys. Metall. Mater. Sci.* 27 (1996) 671–686. <https://doi.org/10.1007/BF02648954>.
- [62] M. Lindroos, T. Pinomaa, K. Ammar, A. Laukkanen, N. Provatas, S. Forest, Dislocation density in cellular rapid solidification using phase field modeling and crystal plasticity, *Int. J. Plast.* 148 (2021) 103139. <https://doi.org/10.1016/j.ijplas.2021.103139>.
- [63] T. Pinomaa, M. Lindroos, M. Walbrühl, N. Provatas, A. Laukkanen, The significance of spatial length scales and solute segregation in strengthening rapid solidification microstructures of 316L stainless steel, *Acta Mater.* 184 (2020) 1–16. <https://doi.org/10.1016/J.ACTAMAT.2019.10.044>.
- [64] X. Feaugas, On the origin of the tensile flow stress in the stainless steel AISI 316L at 300 K: Back stress and effective stress, *Acta Mater.* 47 (1999) 3617–3632. [https://doi.org/10.1016/S1359-6454\(99\)00222-0](https://doi.org/10.1016/S1359-6454(99)00222-0).
- [65] P. Rudolph, Dislocation cell structures in melt-grown semiconductor compound crystals, *Cryst. Res. Technol.* 40 (2005) 7–20. <https://doi.org/10.1002/crat.200410302>.
- [66] N. Ohkubo, K. Miyakusu, Y. Uematsu, H. Kimura, Effect of Alloying Elements on the Mechanical Properties of the Stable Austenitic Stainless Steel., *ISIJ Int.* 34 (1994) 764–772. <https://doi.org/10.2355/isijinternational.34.764>.
- [67] T. Yonezawa, K. Suzuki, S. Ooki, A. Hashimoto, The effect of chemical composition and heat treatment conditions on stacking fault energy for Fe-Cr-Ni austenitic stainless steel, *Metall. Mater. Trans. A Phys. Metall. Mater. Sci.* 44 (2013) 5884–5896. <https://doi.org/10.1007/s11661-013-1943-0>.

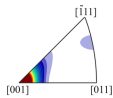
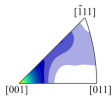
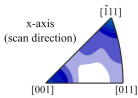
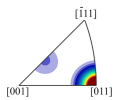
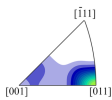
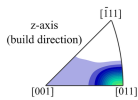
- [68] M. Sudmanns, A.J. Birnbaum, Y. Gu, A.P. Iliopoulos, P.G. Callahan, J.G. Michopoulos, J.A. El-Awady, The interplay of local chemistry and plasticity in controlling microstructure formation during laser powder bed fusion of metals, *Addit. Manuf.* 55 (2022) 102791. <https://doi.org/10.1016/j.addma.2022.102791>.
- [69] P. Deng, H. Yin, M. Song, D. Li, Y. Zheng, B.C. Prorok, X. Lou, On the Thermal Stability of Dislocation Cellular Structures in Additively Manufactured Austenitic Stainless Steels: Roles of Heavy Element Segregation and Stacking Fault Energy, *JOM.* 72 (2020) 4232–4243. <https://doi.org/10.1007/s11837-020-04427-7>.
- [70] Z. Li, T. Voisin, J.T. McKeown, J. Ye, T. Braun, C. Kamath, W.E. King, Y.M. Wang, Tensile properties, strain rate sensitivity, and activation volume of additively manufactured 316L stainless steels, *Int. J. Plast.* 120 (2019) 395–410. <https://doi.org/10.1016/j.ijplas.2019.05.009>.
- [71] Z. Hu, S. Gao, L. Zhang, X. Shen, H.L. Seet, S.M. Ling Nai, J. Wei, Micro laser powder bed fusion of stainless steel 316L: Cellular structure, grain characteristics, and mechanical properties, *Mater. Sci. Eng. A.* (2022) 143345. <https://doi.org/10.1016/j.msea.2022.143345>.
- [72] D.B. Williams, C.B. Carter, *Transmission electron microscopy: A textbook for materials science*, Springer US, 2009. <https://doi.org/10.1007/978-0-387-76501-3>.
- [73] J.H. Hubbel, S.M. Seltzer, *X-Ray Mass Attenuation Coefficients*, (2004). <https://www.nist.gov/pml/x-ray-mass-attenuation-coefficients> (accessed July 21, 2021).



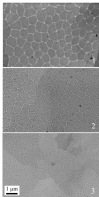
(a)



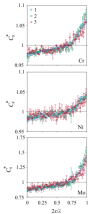
(b)



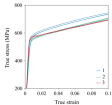
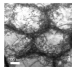
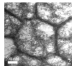
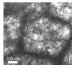
(c)



Different solidification conditions



Similar microsegregations profiles  
Different dislocations patterning



Similar yield strength